Prasanna Hariharan[1]
Food and Drug Administration,
Silver Spring, MD 20993
e-mail: prasanna.hariharan@fda.hhs.gov

Matthew Giarra
Rochester Institute of Technology,
Rochester, NY 14623

Varun Reddy
Pennsylvania State University,
University Park, PA 16802

Steven W. Day
Rochester Institute of Technology,
Rochester, NY 14623

Keefe B. Manning

Steven Deutsch

Pennsylvania State University,
University Park, PA 16802

Sandy F. C. Stewart

Matthew R. Myers

Michael R. Berman

Food and Drug Administration,
Silver Spring, MD 20993

Greg W. Burgreen
Mississippi State University,
Starkville, MS 39762

Eric G. Paterson
Pennsylvania State University,
University Park, PA 16802

Richard A. Malinauskas
Food and Drug Administration,
Silver Spring, MD 20993

Multilaboratory Particle Image Velocimetry Analysis of the FDA Benchmark Nozzle Model to Support Validation of Computational Fluid Dynamics Simulations

This study is part of a FDA-sponsored project to evaluate the use and limitations of computational fluid dynamics (CFD) in assessing blood flow parameters related to medical device safety. In an interlaboratory study, fluid velocities and pressures were measured in a nozzle model to provide experimental validation for a companion round-robin CFD study. The simple benchmark nozzle model, which mimicked the flow fields in several medical devices, consisted of a gradual flow constriction, a narrow throat region, and a sudden expansion region where a fluid jet exited the center of the nozzle with recirculation zones near the model walls. Measurements of mean velocity and turbulent flow quantities were made in the benchmark device at three independent laboratories using particle image velocimetry (PIV). Flow measurements were performed over a range of nozzle throat Reynolds numbers (Re_{throat}) from 500 to 6500, covering the laminar, transitional, and turbulent flow regimes. A standard operating procedure was developed for performing experiments under controlled temperature and flow conditions and for minimizing systematic errors during PIV image acquisition and processing. For laminar ($Re_{throat}=500$) and turbulent flow conditions ($Re_{throat}\geq 3500$), the velocities measured by the three laboratories were similar with an interlaboratory uncertainty of ~10% at most of the locations. However, for the transitional flow case ($Re_{throat}=2000$), the uncertainty in the size and the velocity of the jet at the nozzle exit increased to ~60% and was very sensitive to the flow conditions. An error analysis showed that by minimizing the variability in the experimental parameters such as flow rate and fluid viscosity to less than 5% and by matching the inlet turbulence level between the laboratories, the uncertainties in the velocities of the transitional flow case could be reduced to ~15%. The experimental procedure and flow results from this interlaboratory study (available at http://fdacfd.nci.nih.gov) will be useful in validating CFD simulations of the benchmark nozzle model and in performing PIV studies on other medical device models.
[DOI: 10.1115/1.4003440]

Keywords: particle image velocimetry, computational fluid dynamics, FDA critical path initiative, sudden expansion, shear stress, transitional flow, turbulent flow measurement

1 Introduction

Computational fluid dynamics (CFD) is a technique routinely used to develop and prototype blood-contacting medical devices, such as prosthetic heart valves and ventricular assist devices. CFD results, although not required, are also being used by some manufacturers to help demonstrate safety and efficacy as part of their pre-market device submissions to the U.S. Food and Drug Administration (FDA). Currently, computational methods can be used to simulate both the solid and the fluid mechanics of a device, the transport of blood elements, and the transport and chemical reactions of molecular species. New computational methods are being developed to calculate levels of hemolysis [1–7] and thrombosis [8–12] from the local fluid dynamics derived from simulation using a variety of mathematical methods [13–17]. The advantages of computational studies are that they can provide insight into device performance without having to produce costly prototypes, provide data in regions in which experimental data may not be easy to obtain, and provide data on immeasurable physical quantities. Moreover, with increasing simulation speeds and computational capabilities, CFD methods can be used to evaluate a wide range of physiologic and design parameters and can potentially reduce the extent of animal testing and clinical trials.

However, the use of CFD to demonstrate product safety in FDA pre-market device applications and post-market investigations has not been adequately or systematically validated. This is especially important in the prediction of biological responses (e.g., blood

[1]Corresponding author.
Contributed by the Bioengineering Division of ASME for publication in the JOURNAL OF BIOMECHANICAL ENGINEERING. Manuscript received September 23, 2010; final manuscript received January 8, 2011; accepted manuscript posted January 14, 2011; published online February 17, 2011. Assoc. Editor: David Ku.

damage and thrombus formation) based on the purely physical results (e.g., pressures, velocities, and shear stresses) of the simulations. We initiated a collaborative project to determine the current state and limitations of CFD modeling and the blood damage estimations, as applied to medical devices. The project is part of the FDA's "Critical Path Initiative" program, which is a "national strategy for driving innovation to modernize the sciences through which FDA-regulated products are developed, evaluated, manufactured, and used" [18]. In essence, the goal of our project is to work with the medical device community to improve the use and validation of CFD techniques in medical device evaluation to foster the development of better and safer products and technologies.

In collaboration with researchers experienced in both CFD and particle image velocimetry (PIV) as applied to medical devices, a benchmark nozzle model was developed, which contained features commonly encountered in medical devices (including regions of flow contraction and expansion, local high shear stresses, flow recirculation, and flow regimes that ranged from laminar to turbulent), yet was simple enough that CFD analyses could be readily performed and meaningful comparisons made. By partnering with multiple technical societies, the international CFD community was invited to perform independent simulations of the nozzle model. In response, participants from 28 different groups submitted CFD results [19]. To validate the computational flow simulations, interlaboratory flow visualization experiments at three different laboratories were performed on fabricated physical models. Comparisons of the interlaboratory PIV data allowed us to perform an error analysis, which is a critical component of CFD validation. In addition, to validate the blood damage predictions from the CFD simulations, interlaboratory blood damage experiments were performed at three independent facilities, results of which will be presented in a future report.

This paper addresses three important goals of the FDA CFD blood damage project. The first is to present a benchmark device and an experimental protocol for performing PIV measurements that can be used to validate CFD simulations. The second is to present some noteworthy aspects of the measured data, including some that are particularly subtle and hence deserving of extra attention in CFD validations or further PIV experiments to confirm the results. The third goal is to make these benchmark data available to the scientific community through an online repository for use in future CFD validation studies. The CFD round-robin results as well as the PIV validation of the CFD results will be presented in later publications.

PIV has been widely used in evaluating the performance of medical devices such as artificial heart valves [20–26], blood pumps [27–34], and stents [35,36]. Viscous and Reynolds stresses estimated from PIV have been used to predict the blood damage potential of various medical devices [20,23,25,28,30]. PIV uses an array of computational tools (e.g., cross-correlation algorithms, image processing, and statistics) to estimate the velocity at multiple locations in a flow field. Consequently, the accuracy of the PIV technique depends on the quality of the images, the spatial and temporal image resolutions, and the number of images used, as well as the particle size, particle seeding density, particle displacement, and the ability of the particles to follow the flow. Differences in the PIV algorithms can also significantly influence the accuracy of the predicted flow quantities. An international PIV challenge with more than 23 participating groups[2] investigated the accuracy of different commercial and open-source PIV algorithms by conducting three different round-robin studies with common image sets [37]. A majority of the participants demonstrated the capability of PIV to accurately measure mean (time-averaged) velocities. However, they also acknowledged the limitations of some of the PIV algorithms in measuring turbulent characteristics, as well as velocities and shear stresses for flows near walls [37]. Furthermore, the accuracy and reproducibility of PIV experiments

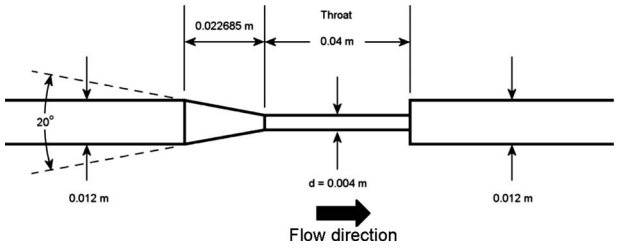

Fig. 1 Benchmark nozzle model: schematic of the test section with dimensions

are affected not only by the algorithms used, but also by experimental factors such as fluctuations in the flow conditions and fluid properties, as well as uncertainties associated with measurements of fluid properties, all of which can vary from one laboratory to another. Controlling these variables to accurately generate the desired flow field is absolutely critical to obtaining accurate estimates of the velocity and stress fields.

To minimize the user error and laboratory bias due to these issues, a standard operating procedure (SOP) for performing the PIV measurements was collaboratively developed in this study. Following the SOP, velocity, pressure, viscous shear stress, and turbulent Reynolds stress data were obtained by the participating laboratories at select cross-sectional locations in the nozzle model. The cross-sections were chosen to appropriately capture the different flow phenomena occurring in the nozzle. Subsequently, an error analysis for the interlaboratory PIV measurements was performed. The error analysis included estimating the uncertainty in the measurements among the laboratories due to differences in PIV algorithms, inlet flow conditions, and fluid property measurements. The combined results from the PIV experiments will be used to evaluate the capability of the CFD simulations to numerically predict the flow fields.

Section 2 describes the benchmark nozzle model and the experimental protocol for the PIV experiments. Uncertainties in the PIV measurements are quantified in Sec. 3.1. Select velocity measurements from all three laboratories are presented in Sec. 3.2. Finally, the applicability of the interlaboratory PIV results for validating the round-robin CFD data is assessed in Sec. 4.

2 Materials and Methods

2.1 Nozzle Model. The benchmark nozzle model is similar to previously reported designs used to compare blood damage computations to experimental data [8,12,38–42]. The model has characteristics of medical devices that have blood flowing through them, including hemodialysis tubing sets, catheters, cannulae, syringes, and hypodermic needles. The nozzle incorporates on one end a 20 deg conical section that gradually reduces the inlet diameter from 12 mm to 4 mm in the nozzle throat; the opposite end is characterized by a sudden increase in diameter (Fig. 1). With flow in one direction, the device resembles a conical concentrator and a sudden expansion (referred to as the "sudden expansion model"). With flow in the opposite direction, the nozzle models a sudden contraction and a conical diffuser (referred to as the "conical diffuser model"). This paper will concentrate on flow through the sudden expansion model, although the experimental results for the conical diffuser model are also available elsewhere.[3]

For performing PIV experiments, three identical nozzle models (one for each of the three laboratories) were fabricated from cast acrylic using an MB-46VAE three-axis computer numerical controlled (CNC) milling machine (Okuma Ace Center, Charlotte, NC). After internal machining and annealing to relieve residual material stresses, the planar external surfaces of the models were

[2]http://www.pivchallenge.org/

[3]http://fdacfd.nci.nih.gov

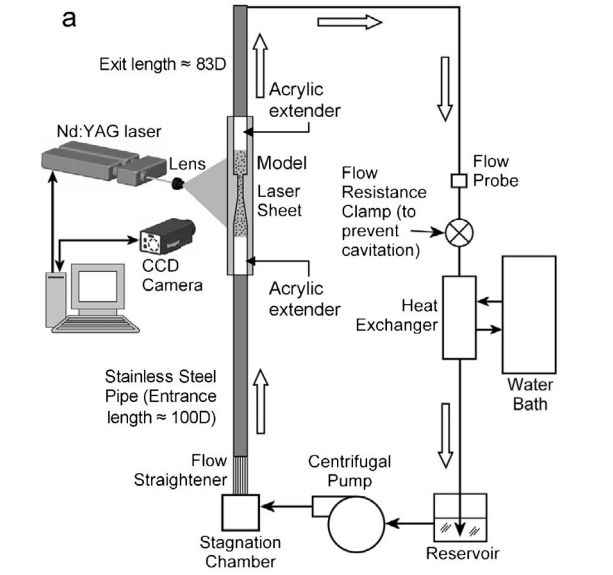

Fig. 2 (*a*) Flow loop for sudden expansion configuration. Laboratory specific operating conditions are listed in Table 3. (*b*) Picture of the nozzle and the acrylic extenders.

hand-polished to provide clear optical access to the internal geometry. Internal features of the test section were then hand- and vapor-polished to meet specifications. Quality control of the test sections was performed using gauge pins, a metrology rubber, and an optical comparator. All nozzle dimensions (inlet, exit, and throat diameters) were maintained within 1% of the specifications. The root-mean-square (rms) roughness of the inner surface was measured to be less than 5×10^{-4} mm. The radius of curvature of the sharp corner at the sudden expansion (i.e., where the nozzle diameter increases abruptly from 4 mm to 12 mm) was measured to be less than 0.025 mm. For performing pressure measurements, a separate acrylic model was made with 17 counter-bored pressure taps (with a diameter of 0.56 mm) drilled radially along the length of the model.

2.2 Flow Loop. Figure 2 shows the schematic of the flow loop used in the flow visualization and pressure measurement experiments. The nozzle model was fitted with acrylic extenders and stainless steel pipes on either end to ensure straightness and fully developed flow at the nozzle inlet. The acrylic extenders were glued to the main model using chemical welding, and epoxy was used to glue the stainless pipes to the extenders. The entrance region was approximately 120 cm long (i.e., 100D, where D is the inlet pipe diameter of 1.2 cm). The acrylic extender on the outlet side allowed the flow field downstream of the nozzle to be visualized up to a distance of 16D. The exit length was approximately 100 cm (i.e., 83D), which was intended to prevent the outlet flow condition from influencing the reattachment point in the model.

A centrifugal pump was used to draw fluid from the reservoir and push it through the model. The fluid temperature and, therefore, viscosity were held constant, either by using an inline heat exchanger or by placing the fluid reservoir in a water bath. A stagnation chamber was used to decelerate and mix the incoming fluid. This mixing chamber also helped to eliminate asymmetries in the inlet velocity profile caused by secondary flows due to the curvature of the connector tubes. A flow straightener (consisting of a bundle of 13 0.25 cm diameter tubes placed co-axially to the flow) was located between the stagnation chamber and the inlet pipe to disrupt residual disturbances in the flow before it entered the test section. An ultrasonic flow probe mounted upstream of the heat exchanger was used to monitor the flow rate.

The Newtonian blood analog fluid for the PIV experiments was composed of 50 wt % saturated aqueous sodium iodide (NaI) solution, 20 wt % glycerin, and 30 wt % water. The blood analog fluid was formulated to match the refractive index of the acrylic ($\sim$1.49) and to make the model optically transparent to the laser and the camera. Table 1 summarizes the properties of the blood analog fluid prepared and measured by each of the laboratories. Density was measured either by weighing a known volume of the test fluid (200 ml) in a precision weighing balance or by using a density meter (DMA 35, Anton Paar, Austria). The refractive index was measured using a digital handheld refractometer (PA202, Palm Abbe, Cleveland, OH). Different types of viscometers were used to measure the viscosity of the fluid (Table 1). A glycerin-water mixture (40/60 wt %) was used as the blood analog fluid during the pressure measurements since the index of refraction mismatch was not a potential source of error. The viscosity and density of the blood analog fluid used in pressure measurements are listed in Table 1. The flow rate was adjusted during each experiment to match the specified Reynolds number (500, 2000, 3500, 5000, or 6500). The Reynolds number (Re_{throat}) was calculated based on the nozzle throat diameter (Fig. 1) and the average throat velocity. The corresponding Reynolds number at the inlet and exit pipes would be one-third of the Re_{throat} value.

2.3 PIV System. The PIV systems (Table 2) incorporated a double-pulsed Q-switched multimode neodymium doped yttrium aluminum garnet (Nd:YAG) laser (λ=532 nm), with a beam diameter of $\sim$2.5 mm and a repetition rate of 8–15 Hz as the illu-

Table 1 Properties of the blood analog fluids, measured before each PIV trial. The table lists the range measured by each laboratory. Flow rate was adjusted according to changes in fluid properties to maintain a constant Reynolds number. Shear rates at which the viscosities were measured are as follows: Lab-1=10–75 s^{-1}, Lab-2=100–1000 s^{-1}, and Lab-3=245 s^{-1}.

		Sodium iodide solution (PIV experiments)			Glycerin-water mixture (for pressure measurements)	
Laboratory	Viscometer	Dynamic viscosity (cP)	Specific gravity	Refractive index	Dynamic viscosity (cP)	Specific gravity
Lab-1	DV-E (Brookfield Engineering Laboratories, Inc., Middleboro, MA)	6.74–7.60 (at 21 °C)	1.68–1.72	1.485	3.6	1.06
Lab-2	Vilastic (Vilastic Scientific Inc., Austin, TX)	6.90 (at 25 °C)	1.66–1.77	1.485	3.46	1.15
Lab-3	DV-III (Brookfield Engineering Laboratories, Inc., Middleboro, MA)	7.58–7.77 (at 21 °C)	1.73	1.486	3.7	1.05

Table 2 Specifications for the PIV systems used by the participating laboratories

Lab	PIV processing software	CCD camera	CCD size (pixels)	Image depth (bits/channel)	Recording rate (Hz)
Lab-1	DAVIS FLOWMASTER (LaVision Inc., Ypsilanti, MI)	Lavision Imager Pro X	1600×1200	12	1–8
Lab-2	INSIGHT 3G (TSI, Inc., Shoreview, MN)	TSI PIVCAM 14-10	1376×1024	16	1–8
Lab-3	WIDIM [65]	IDT Motion Pro X3 Plus (IDT Inc., Tallahassee, FL)	1280×1024	11	~5

mination source. The laser beam was passed through an optical arrangement to convert the laser beam into a thin laser sheet (0.5–0.6 mm thickness) for planar illumination of the flow in the model. The fluid medium was seeded with 10 μm hollow glass spheres (~0.2 g/l; Lavision, Göttingen, Germany) to act as tracer particles for visualizing the flow. The specific gravity of the spheres was approximately 1.1, while that of the fluid was 1.67–1.77. Flow visualization and image collection were done using a charge coupled device (CCD) or complementary metal oxide semiconductor (CMOS) camera, which was connected to a computer that stored and processed the recorded images (Table 2). The computer also communicated with a delay generator that synchronized the camera with the laser source.

2.4 Standard Operating Procedure. This section describes the SOP developed for the flow visualization experiments. The goals of the SOP were to (i) develop a *standard protocol for the experimental setup* that ensured a fair comparison with the CFD simulations by creating similar operating and boundary conditions in the PIV experiments (such as parabolic inlet flow, flow symmetry, minimal fluctuations in flow rates and fluid properties, i.e., constant Reynolds number, and absence of cavitation) and (ii) develop a list of *best practices* for the PIV measurements based on the techniques described in the literature to minimize PIV processing errors and improve interlaboratory reproducibility. Table 3 provides a comparison of the experimental operating conditions between the three participating laboratories.

2.4.1 Standard Protocol for Experimental Setup

Model orientation. The test section was always oriented vertically, as shown in Fig. 2. Vertical orientation was necessary to avoid bubbles and tracer-particle debris settling at the low-flow recirculation region near the sudden expansion region, which occurred when the test section was horizontal.

Fluid temperature. The temperature of the blood analog fluid was maintained at a constant, within ±0.5°C (Table 3) using a heat exchanger, to avoid fluctuations in fluid properties. If left unregulated, the temperature of the fluid tended to increase with time due to heat generated by the pump. A temperature increase of 5°C corresponds to a decrease in fluid viscosity of approximately 1 cP (~15% of nominal). By controlling the fluid temperature and properties, a less than ~1% fluctuation in flow rate was observed during the experiments (Table 3).

Fluid properties. To ensure proper control of the flow conditions, the dynamic viscosity and density of the fluid were measured before each PIV measurement. The flow rate was adjusted according to the fluid property variations to maintain a constant

Table 3 Comparison of the interlaboratory PIV experimental configurations and practices

Experimental parameter		Lab-1	Lab-2	Lab-3
		Standard protocol		
Temperature control		Inline heat exchanger	Water bath	Water bath
Temperature fluctuations (°C)		±0.2	±0.5	±0.2
Flow rate fluctuations (%)		<1	<1	<1
Occurrence of cavitation		No	No	No
Inlet flow condition (flow asymmetry)		Eliminated using flow straightener and settling chamber (SI: 0.93–1)	Eliminated using flow straightener and settling chamber (SI: 0.93–1)	Eliminated using flow straightener and settling chamber (SI: 0.93–1)
Inlet flow profile	Re_{throat}=500–5000	Poiseuille flow	Poiseuille flow	Poiseuille flow
	Re_{throat}=6500	Laminar and developing	Turbulent	Turbulent
		Best practices		
Particle image size (pixels)		~2	~2	~2
Particle seeding density (number of particles/interrogation window)		>10	>10	>10
Laser sheet thickness (mm)		0.6 (scanning pinhole profiler method)	0.5 (burn paper method)	0.5 (burn paper method)
Pixel resolution (μm)		9–11	11	13.7
Interrogation window size (pixels)		32×32 (50% overlap)	32×32 (50% overlap)	32 axially×16 radially (50% overlap)
Mesh size (final PIV resolution)		0.144–0.176 mm	0.176 mm	0.219×0.11 mm^2
Δt between images—adherence to the one-quarter rule (in the jet)		Yes	Yes	Yes
Δt between images—adherence to the one-quarter rule (in the low-flow recirculation region)		Yes	No	No
Number of image pairs		Laminar: 500; turbulent: 1000–2500	Laminar: 500; turbulent: 1000	Laminar: 500; turbulent: 1000

Reynolds number. To ensure accuracy in flow rate measurement, the ultrasonic flow meter was calibrated before every measurement using a graduated cylinder and stopwatch. The refractive index of the fluid was measured before each experiment and adjusted accordingly (by adding small amounts of NaI or water) to match the refractive index of acrylic.

Cavitation effects. The flow loop was designed to avoid cavitation in the pump and the test section. Cavitation can occur at the location of the sudden contraction (in the conical diffuser model) where the diameter of the model decreases abruptly from 12 mm to 4 mm. The sudden increase in velocity at the sharp-edged contraction is accompanied by a decrease in pressure, which may decrease below the fluid vapor pressure depending on the inlet pressure and flow rate, the corner sharpness, and other factors. Cavitation was prevented by applying a flow restriction downstream of the model in order to increase the pressure within the model; care was taken not to overpressurize the model. In addition, to avoid low pressure conditions and cavitation, the model was always placed on the discharge side of the pump (Fig. 2).

Inlet boundary condition. The flow loop was designed to obtain a fully developed flow boundary condition at the inlet for the majority of the flow conditions. While the long entrance length ($\sim$100D) ensured fully developed flow at the entrance for most flow rates, care was also taken to ensure that the velocity profile across the inlet tube cross-section was symmetric. Use of the stagnation chamber and flow straightener combined with proper alignment of the inlet tubing helped to avoid secondary flows and asymmetric inlet velocity profiles. Before collecting data at locations downstream of the inlet, the symmetry of the inlet velocity profile was measured. A detailed discussion of the inlet velocity profiles is provided in Sec. 3.1. It should be noted that the inlet and exit boundary conditions were not specified in the CFD round-robin study, and the participants were given the freedom to choose the boundary conditions based on their individual judgments.

2.4.2 Best Practices for PIV Measurements. This section lists the best practices that were followed for making velocity measurements using the PIV technique. These rules were formulated following guidelines from previous PIV studies [43–55]. The rationale for the selection of the key PIV parameters, which are also summarized in Table 3, is as follows:

1. *Particle size and pixel resolution:* Particle image size was kept large enough to avoid bias error due to the peak locking effect. Peak locking occurs when estimating the particle displacement to subpixel accuracy using various curve-fitting methods. Since the cross-correlation operation to estimate the particle displacement is performed on a digitized image field, the resolution of the estimated displacement cannot be less than a pixel (for no window overlap; 0.5 pixel for 50% overlap). Consequently, the majority of the cross-correlation algorithms use different types of curve-fitting methods to obtain subpixel resolution during displacement estimation; the main drawback of using such algorithms is that they can introduce significant bias error when the particle images are under-resolved [49]. When the particle image size is too small (<2 pixels), the particle displacement calculated with the subpixel estimators is always biased toward the nearest integer-valued pixels (i.e., for a true displacement of 2.3 pixels, the algorithm will lock the displacement to 2 pixels). To eliminate this bias error due to peak locking, previous studies have shown that the particle image diameter should be $\sim$2 pixels [44,46] and should never be <1 pixel.
2. *Particle density:* To increase the signal to noise ratio in the PIV cross-correlation results and to reduce the measurement uncertainty, the total number of particles in an interrogation window exceeded 10 [46–48].
3. *Laser sheet:* The following steps were taken to minimize inaccuracies in PIV measurement due to variations in the intensity of tracer particles between consecutive images [50].
   (a) By adjusting the laser intensities, we ensured that the two images obtained from both laser pulses (making an image pair) received equal amounts of illumination.
   (b) We also ensured that the light sheets from the pulsed laser beams overlapped. Frequent realignment was required to keep the sheets coplanar. This prevented intensity variations between particles in the image pairs and also prevented the appearance or disappearance of particles from the laser sheet, both of which can introduce large errors in the displacement calculation [50]. This was confirmed by observing image pairs in a stagnant flow, which should appear nearly identical.
   (c) The thickness of the laser sheet was measured periodically to ensure that it was thin enough to avoid spatial velocity averaging through the sheet thickness [51]. In this study, laser sheet thickness was measured either by the scanning pinhole profiler method [52] or by using burn paper and was found to be less than 0.6 mm (Table 3).
4. *Frame separation* (Δt) *and particle displacement limit:* The temporal separation, Δt, between the two frames of a PIV image pair was appropriately chosen to decrease the relative uncertainty of the measurement by making the measured displacement large compared with the absolute uncertainty (0.1–0.2 pixels) of the displacement measurement. To avoid tracer particles traveling outside the interrogation window resulting in lost correlation between image pairs, the Δt was chosen such that the peak particle displacement (in the jet) was less than or equal to 0.25 times the initial interrogation window size (i.e., the one-quarter particle displacement rule [53]). Actual Δt values varied depending on the flow rate, the local velocity, the camera resolution, and the need to reduce the out-of-plane motion of the particles. For example, the Δt values used by Lab-1 for $\mathrm{Re}_{\mathrm{throat}}=500$ were 1400 μs, 395 μs, and 1500 μs, for the entrance, throat, and recirculation regions in the model. In some regions, we also had to adjust the Δt to accommodate flows with large velocity gradients across the field of view. An example of such a situation is the sudden expansion region in the nozzle model (Fig. 1) where the recirculation velocities adjacent to the jet can be as low as 2–10% of the jet velocity. Here, it was necessary to collect data in the two regions separately, at a small Δt for jet velocity measurement (e.g., 200 μs) and at a large Δt for low velocity in the recirculation regions (e.g., 1000 μs).
5. *Number of image pairs:* The number of image pairs collected for measurement depended on the statistics that needed to be performed and on the nature of the flow. Highly turbulent flows required collecting a large number of image pairs [54,55]. For laminar flow in the nozzle, we captured up to 500 image pairs based on our experience with similar flows. However, for turbulent flows, we increased the number of image pairs until the mean velocity and the statistical quantities became independent of the image count. A convergence study was conducted in which mean velocity (time averaged) and turbulent statistics (i.e., Reynolds stresses) were obtained for 200, 600, 1000, and 1200 image pairs at $\mathrm{Re}_{\mathrm{throat}}=6500$. The mean velocity measured by the different image counts matched one another within $\sim$1%, suggesting that less than 200 image pairs were required to obtain convergence in the mean velocity. However, the Reynolds stresses obtained for 200 image pairs differed by $\sim$70% in comparison with the values obtained with 1000 and 1200 image pairs, suggesting that more than 1000 image pairs were required to obtain an image-count independent

Table 4 Positive control experiment to evaluate errors accrued by not adhering to the PIV best practice procedures. While performing the control experiments, all the protocol violations were made simultaneously.

Experimental setup	Adhering to SOP (Lab-1)	Not adhering to SOP
Entrance length	100D (D: inlet pipe diameter=12 mm)	40D
Temperature control	Inline heat exchanger	No
Temperature fluctuations	±0.2°C	4°C increase in 10 min
Flow rate fluctuations	None (Re_{throat}=500–5000);0.5% drift at Re_{throat} =6500	3% drift at Re_{throat}=6500
Inlet flow conditions (flow asymmetry)	Eliminated using flow straightener and settling chamber	No flow straightener or settling chamber used
Inlet flow profile	Poiseuille flow for Re_{throat}=500; laminar, developing, and symmetric for Re_{throat}=6500 (SI: 0.93–1)	Asymmetric flow for Re_{throat}=500 and 6500 (SI: 0.75–0.85)
Particle image size (pixels)	>2	~1
Particle seeding density (number of particles/interrogation window)	>10	<10
Laser sheet thickness (mm)	0.6	~3
Maximum pixel displacement	16 pixels (initial interrogation window size =64 pixels)	3 pixels (interrogation window size =16 pixels)
Δt between images—adherence to the one-quarter rule (in the jet)	Yes	No
Number of image pairs	Laminar: 500; turbulent: 1000–2500	Laminar: 100; turbulent: 100

estimate of statistical quantities such as the Reynolds stresses.

2.5 Evaluation of PIV Procedures. In order to evaluate the overall sensitivity of various flow parameters to the SOP, a set of positive control experiments was performed at Lab-1. Velocity measurements were made while violating various aspects of the PIV procedures, as listed in Table 4. It should be noted that all protocol violations in Table 4 were made simultaneously and not individually. The results showed that each flow quantity exhibited a different level of sensitivity to the SOP conditions (Fig. 3). For example, the centerline velocity demonstrated a ~20% error when not following the protocol (Figs. 3(*a*) and 3(*b*)). Similarly, the flow rate calculated from integrating (radially) the measured axial velocity profiles in Figs. 3(*a*) and 3(*b*) was ~25% below the flow rate measured by the flowmeter. The spatial averaging of the measured velocity due to a thicker laser sheet and asymmetric flow due to the absence of a flow straightener and mixing chamber (Table 4) could have contributed to this variation. The correspond-

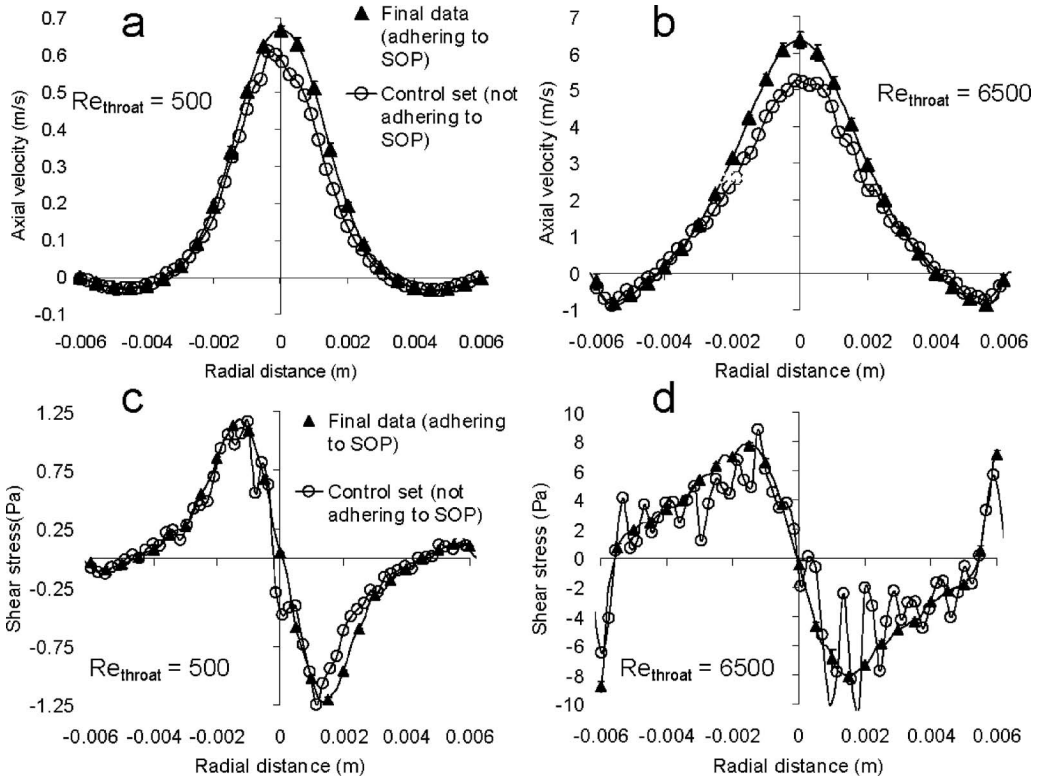

Fig. 3 Sensitivity of flow variables to the standard operating procedure. ((*a*) and (*b*)) Axial velocity as a function of radial distance for Re_{throat}=500 and 6500. ((*c*) and (*d*)) Viscous shear stress profile for Re_{throat}=500 and 6500. (○) Positive control (with SOP violations); (▲) final data (SOP followed).

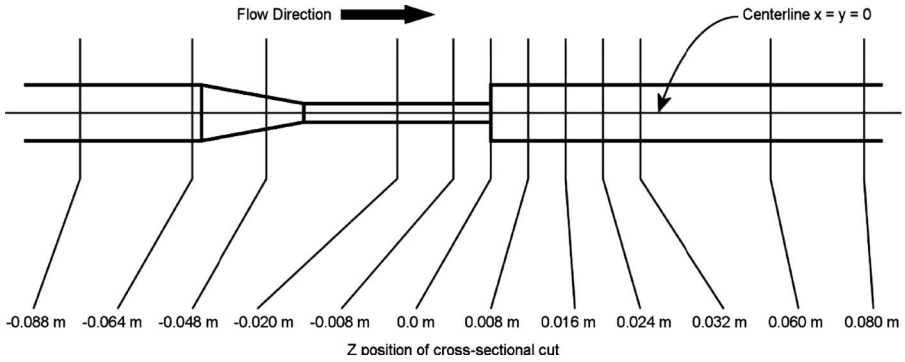

Fig. 4 Schematic of the test section showing the locations where velocity, shear stress, and Reynolds stresses were measured for the sudden expansion orientation

ing calculations of fluid shear stress were even more error prone with ~30% and ~70% errors estimated in the peak viscous stress (Figs. 3(*c*) and 3(*d*)) and Reynolds stress when not adhering to the protocol. In addition, since the shear stress for the positive control experiments was estimated from finite differencing of the noisy and peak-locked velocity data (Figs. 3(*a*) and 3(*b*)), radial shear stress profiles for the control group were wavy and jagged, with the error at the off-peak locations exceeding ~70% (Figs. 3(*c*) and 3(*d*)).

2.6 Comparison Metrics. The flow fields were characterized at 12 different cross-sections (Fig. 4), so that parameters relevant to blood damage (viscous and Reynolds shear stresses and blood cell dwell times) could be calculated and compared at specific locations. The metrics for comparing CFD simulations to PIV data included (i) centerline velocity, (ii) jet width at the nozzle exit, (iii) axial velocity versus radial distance, (iv) radial velocity versus radial distance, (v) viscous shear stress magnitude versus radial distance, (vi) Reynolds stress magnitude versus radial distance, (vii) wall shear stress, and (viii) pressure along the wall.

For each flow condition, three trials were conducted at Lab-1 and one each at Lab-2 and Lab-3 following the standard operating procedure described in the previous section (Table 3). The three trials at Lab-1 were conducted independently of one another on different days using a fresh batch of blood analog fluid. The flow loop was dismantled and reassembled before each trial. When estimating the interlaboratory mean and standard deviation for the experimental data, only the averaged value from the three Lab-1 trials was used (not the individual Lab-1 trials) to avoid biasing the mean toward Lab-1 data. Since the fluid properties were different for the five experimental trials (Table 1), the flow rates were varied to maintain a constant Reynolds number. The CFD simulations were carried out using nominal blood properties (dynamic viscosity (μ_{blood})=3.5 cP and density (ρ_{blood})=1.056 g/cm^3). Therefore, all flow quantities from PIV experiments were scaled to CFD conditions using Reynolds number similarity:

$$u_{blood} = u_{NaI} \times \left(\frac{\mu_{blood}\rho_{NaI}}{\mu_{NaI}\rho_{blood}} \right) \quad (1)$$

$$\tau_{blood} = \tau_{NaI} \times \left(\frac{\mu^2_{blood}\rho_{NaI}}{\mu^2_{NaI}\rho_{blood}} \right) \quad (2)$$

$$\tau'_{blood} = \tau'_{NaI} \times \left(\frac{\mu^2_{blood}\rho_{NaI}}{\mu^2_{NaI}\rho_{blood}} \right) \quad (3)$$

where μ_{NaI} and ρ_{NaI} are the viscosity and density of the blood analog fluid and u_{NaI}, τ_{NaI}, and τ'_{NaI} are the velocity, viscous shear stress, and Reynolds stress measured or calculated from PIV experiments, respectively. The subscripts denote whether the values are for blood or NaI. This paper focuses primarily on the velocity and pressure measurements made in the nozzle model. The viscous and Reynolds shear stress data will be evaluated in future studies.

3 Results

3.1 Error Analysis. This section quantifies uncertainties in the interlaboratory measurements due to differences in the flow parameters and measurement errors not overcome by following the SOP. The error analysis was critical in explaining some of the deviations in the interlaboratory velocity data, which are presented in Sec. 3.2. Uncertainties in flow and pressure parameters are expressed in terms of either the standard deviation or the coefficient of variation.

Fluid property measurements. While fluid property measurement equipment (e.g., viscometers) are periodically calibrated, equipment-specific measurement inaccuracies between laboratories can still exist. To account for this variability, a single batch of blood analog fluid (made at Lab-1) was tested simultaneously in all three laboratories. Over the range of tested shear rates, the standard deviations of the viscosity measurements from the three laboratories (calculated at 21 °C and 25 °C) were within 5% of the mean. Since the flow rates for experiments were adjusted based on the fluid properties, a 5% uncertainty was introduced in the Reynolds number and the inlet velocity due to inaccuracies in fluid property measurement.

PIV algorithm. Variations in the calculated experimental velocities could also be caused by differences in the PIV algorithms used by the laboratories. To account for this variation, we carried out a comparison study similar to the one conducted by Stanislas et al. [37] in the international PIV challenge. All three laboratories used their respective PIV algorithms (Table 2) to process the same set of 100 image pairs. The images were obtained for Re_{throat} =6500 at a location immediately downstream of the sudden expansion (at z=0.008 m in Fig. 4). Figure 5 shows a comparison of the mean velocity, viscous shear, and Reynolds stresses estimated by the laboratories for the same set of images. The interlaboratory variations in peak velocity and viscous shear stress were less than 1% and 6%, respectively. However, the uncertainty in peak Reynolds stress value was more, around 15%.

Inlet boundary condition. Since variations in the inlet boundary conditions (i.e., the inlet axial velocity profile) can affect the downstream flow field, care was taken to maintain a uniform inlet condition among the laboratories (Table 3). Variability in the inlet boundary condition was quantified by comparing the measured inlet velocity profiles to those for a fully developed flow profile assuming Poiseuille flow. In comparison to the Poiseuille flow profile, fully developed laminar flow was attained for all flow conditions except at Re_{throat}=6500 (Figs. 6(*a*) and 6(*b*)), which corresponded to an inlet Re of 2176. For Re_{throat}<6500, peak velocity from the laboratories matched with each other within ~10%. Consequently, variations in inlet boundary conditions among the laboratories were expected to introduce ~10% uncer-

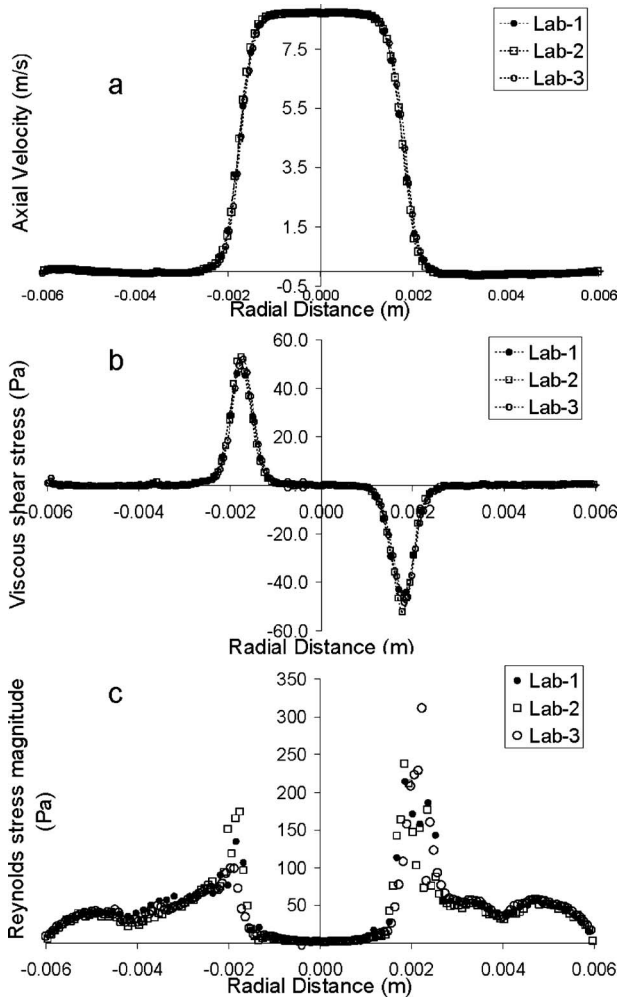

Fig. 5 Uncertainty analysis comparing PIV software using the same 100 image pairs supplied by Lab-1. Interlaboratory comparison of (*a*) mean axial velocity, (*b*) viscous shear stress, and (*c*) Reynolds stress magnitude. Images for this comparison study were obtained for $Re_{throat}=6500$. PIV data obtained at z =0.008 m (Fig. 4).

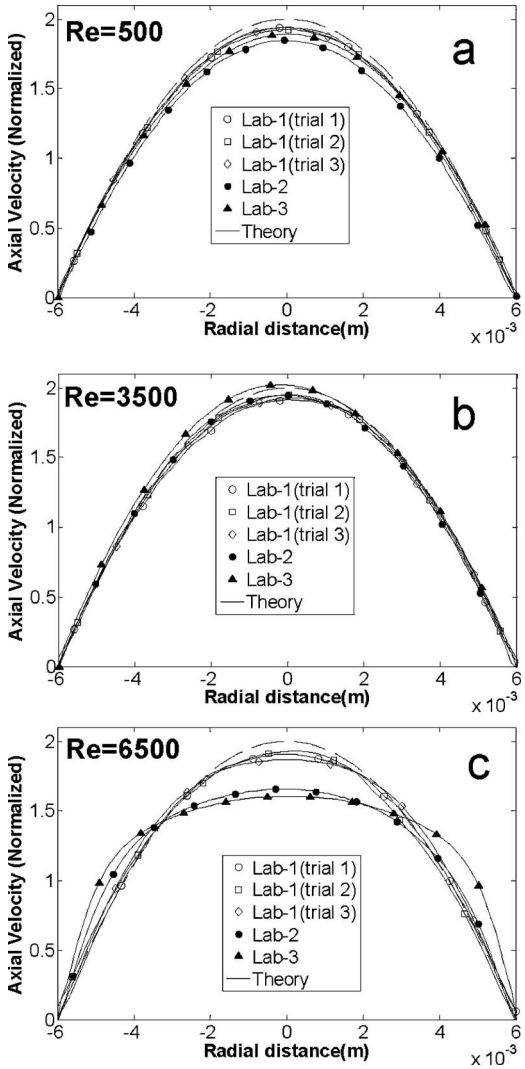

Fig. 6 Axial velocity profile at the entrance (z=−0.064 m in Fig. 4) for $Re_{throat}=500$, 3500, and 6500. The corresponding velocity profiles for the Poiseuille flow are also included.

tainty in the Reynolds number at which the flow measurements were made. Further, the interlaboratory mean of the peak velocity matched within ~5% of the peak velocity calculated for the Poiseuille flow. This was expected as the inlet Reynolds numbers for all the flow rates for a $Re_{throat}<6500$ were in the laminar flow regime (the Re_{inlet} is one-third of the Re_{throat}).

In contrast, for $Re_{throat}=6500$, the Re_{inlet} of ~2167 is in the transitional flow regime. The flow was still laminar but not fully developed for the three Lab-1 trials (Fig. 6(*c*)). However, unsteady transitional or turbulent flow was observed by the other two laboratories. At the inlet, the Reynolds number (Re_{inlet}) at which the flow transitioned from the laminar to the turbulent regime was different for each laboratory. This was confirmed by comparing the rms of the fluctuating axial velocity at z=−0.064 m (Fig. 7). For $Re_{inlet}=2167$, the rms velocity values for Lab-1 trials were less than 4% of the mean velocity. In contrast, the peak rms values for the other two laboratories were >15% of the mean velocity. Thus, any large variations in the downstream velocity profiles among the laboratories at the transitional flow regime (i.e., at $Re_{inlet}=2167$) could be a result of this difference.

The symmetry of the entrance flow profile was evaluated by calculating the flow rate from the experimental velocity profile about both sides of the vertically oriented axial centerline. A symmetry index (SI) was calculated as

$$SI=\begin{cases}\dfrac{\text{Flow rate (left half)}}{\text{Flow rate (right half)}} & \text{if } Q_{\text{left half}}<Q_{\text{right half}}\\[2ex] \dfrac{\text{Flow rate (right half)}}{\text{Flow rate (left half)}} & \text{if } Q_{\text{left half}}>Q_{\text{right half}}\end{cases} \quad (4)$$

The orientation of the upstream stagnation chamber, the flow straightener, and the inlet tubing was adjusted to attain the maximum possible SI value of 1 at the model entrance for each flow rate. For all of the laboratories, the SI varied between 0.97 and 1 for $Re_{throat}=500$, 2000, and 3500 and between 0.93 and 1 for $Re_{throat}=5000$ and 6500. Consequently, little variation in the downstream mean velocity profiles was expected due to inlet flow asymmetry.

3.2 Velocity and Pressure Profiles With Sudden Expansion at Exit

3.2.1 Laminar and Turbulent Flow Regimes ($Re_{throat}=500$, 3500, 5000, and 6500). In general, when the flow in the throat was laminar or turbulent, the velocities measured by the laboratories were similar and varied by ~10%. Figure 8 shows the variation in

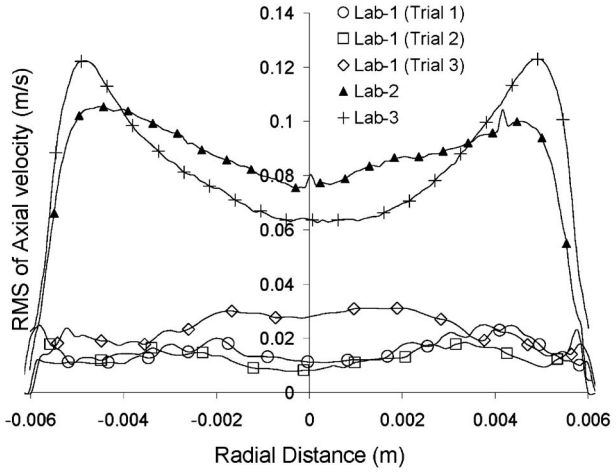

Fig. 7 Turbulence quantified by the rms of axial velocity fluctuations versus radial distance at the nozzle inlet (z= −0.064 m in Fig. 4) for Re_{throat}=6500. Mean velocity for this Reynolds number=0.6 m/s.

centerline velocity and pressure difference (measured near the wall) along the length of the nozzle model at the predetermined locations. All velocity data were normalized with respect to the average velocity at the inlet,

$$\bar{u}_{inlet} = \frac{Q}{\pi r_{inlet}^2} \tag{5}$$

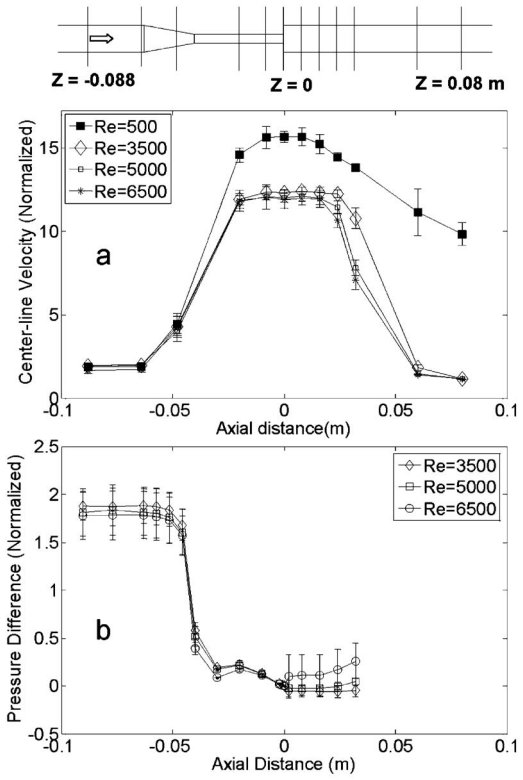

Fig. 8 Sudden expansion orientation: (*a*) centerline velocity (normalized to the mean inlet velocity) versus axial distance for different flow conditions; (*b*) pressure difference (normalized to the mean throat velocity) versus axial distance. Pressure difference normalized based on Eq. (8). Mean and standard deviations were calculated from three Lab-1 trials (averaged) and one trial each from Lab-2 and Lab-3 (n=3).

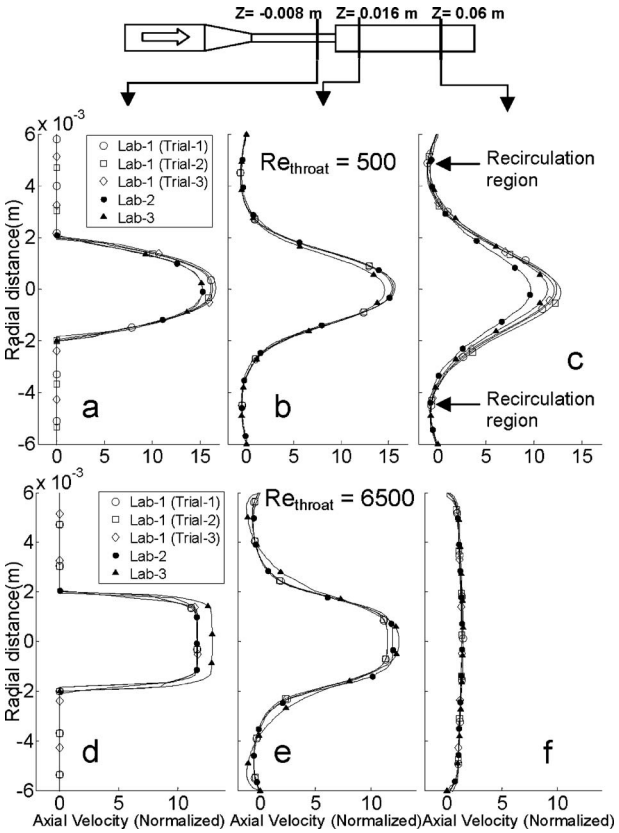

Fig. 9 Sudden expansion orientation: velocity profiles at different cross-sections for two Reynolds numbers (500 and 6500), normalized to the mean inlet velocity. Example recirculation regions are identified with arrows in (*c*).

$$u_{normalized} = \frac{u_{blood}}{\bar{u}_{inlet}} \tag{6}$$

where Q is the experimentally measured volumetric flow rate, r_{inlet} is the inlet pipe radius=6 mm, r_{throat} is the throat radius=2 mm, and $\bar{u}_{inlet}$ is the mean inlet velocity.

All pressure difference data were normalized with respect to the average velocity at the throat,

$$\bar{u}_{throat} = \frac{Q}{\pi r_{throat}^2} \tag{7}$$

$$\Delta P_{normalized} = \frac{\Delta P}{1/2\rho_{blood}\bar{u}_{throat}^2} \tag{8}$$

where ΔP is the pressure difference measured relative to the pressure at z=0 (Fig. 4) ($\Delta P = P_z - P_{z=0}$) and $\bar{u}_{throat}$ is the mean throat velocity calculated from the volumetric flow rate. Axial velocity profiles measured at select radial cross-sections for Re_{throat}=500 and 6500 are shown in Fig. 9.

Entrance region and throat. For flow rates corresponding to Re_{throat}=500–5000, the flow entering the model (measured at the axial position z=−0.064 m in Fig. 8(*a*)) was fully developed for the three laboratories with the normalized centerline velocity identical and equal to twice the normalized inlet average velocity (=1). The flow then accelerated in the conical concentrator section due to the decrease in the cross-sectional area. The majority of the drop in static pressure, ~70% of the total drop, occurred in the conical concentrator section of the nozzle (Fig. 8(*b*)), part of which was due to the conversion of potential energy to kinetic energy. The fluid pressure continued to drop gradually, due to viscous losses, in the throat section where the flow started to

redevelop. For $Re_{throat}=500$, the throat was not long enough to re-establish fully developed flow. Consequently, the normalized centerline velocity measured in the throat region (~ 16) was less than the value expected for the corresponding fully developed flow condition ($=(r_{inlet}/r_{throat})^2 \times u_{normalized\ at\ inlet}=18$). For $Re_{throat}>3500$, the measured centerline velocity in the throat (~ 12) matched well with the values reported in the literature for fully developed turbulent flows [56]. For $Re_{throat}=6500$, the centerline velocity in the throat region for Lab-1 and Lab-2 matched each other within $\sim 2\%$ (Fig. 9(*d*)). However, the throat velocity for Lab-3 was $\sim 10\%$ more than the other two laboratories. Since the velocity profile is almost uniform across the throat radius (Fig. 9(*d*)), this upward shift in the plug velocity indicates a corresponding increase in the flow rate. When the flow rate was calculated by integrating the radial velocity profile, a $\sim 9\%$ increase was observed for Lab-3 in relation to the other laboratories. The sources for this variation, as discussed in Sec. 3.1, are the differences in fluid property measurements and inlet boundary conditions between the laboratories. The cumulative error introduced by these sources was around $\sim 10\%$.

Sudden expansion region. Upon exiting the nozzle throat into the sudden expansion region, the flow separated from the wall forming a high speed jet in the core with a low-flow recirculation zone near the wall region (Figs. 9(*b*), 9(*c*), and 9(*e*)). Immediately downstream of the sudden expansion (between z=0 to 0.032 m (Fig. 8(*a*))), good agreement was obtained among laboratories in the jet velocity measurement, with the interlaboratory uncertainty around $\sim 10\%$. The peak velocities in the recirculation eddies were less than one-tenth those of the jet (Fig. 9(*c*)). While the jet was symmetric about the nozzle axis, a slight asymmetry in the strength of the recirculation eddies was observed for all flow conditions (Figs. 9(*b*), 9(*c*), and 9(*e*)).

Reattachment region. For all $Re_{throat}>500$ conditions, the flow was observed to reattach to the wall within 20H, where H (=4 mm) is the step height or difference between the exit pipe radius and the throat radius. For $Re_{throat}=500$, reverse flow was measured near the wall at the last measurement location i.e., z =0.08 m, suggesting that the reattachment occurred at a z >20H. This is in agreement with observations made in previous studies [57] where the reattachment lengths in similar nozzle models at similar Reynolds numbers were observed to be $\geq$20H.

For the turbulent flow conditions ($Re_{throat}\geq 3500$), the reattachment point occurred closer to the expansion step (between 8H and 15H) than for the laminar and the transitional cases. However, the recirculation length did not change with an increase in Reynolds number as the flow became fully turbulent. The interlaboratory uncertainties in the centerline velocity measurements near the reattachment region for $Re_{throat}\geq 3500$ were less than $\sim 8\%$ (at z =0.032 m in Fig. 8(*a*) and Fig. 9(*e*)).

Post-reattachment region. For the turbulent flow conditions ($Re_{throat}\geq 3500$), once the jet expanded and reattached to the wall, the entire pipe was filled with forward moving flow, thus reducing the centerline velocity to the level of the inlet average velocity, i.e., half of the inlet centerline velocity (as indicated by Fig. 9(*f*) and the last two data points in Fig. 8(*a*)).

3.2.2 Transitional Flow Regime ($Re_{throat}=2000$). In the transitional flow regime ($Re_{throat}=2000$), the interlaboratory velocity data agreed with each other within $\sim 15\%$ at the entrance, conical concentrator, throat, and sudden expansion regions of the nozzle (Figs. 10, 11(*a*), and 11(*b*)). However, downstream of the sudden expansion region, near the reattachment region, velocity profiles from the three laboratories were significantly different from one another (Figs. 10 and 11(*c*)). The rms velocities from Lab-1 trials (measured just before the reattachment region at z=0.032 m) were three to four times lesser than the values measured by Lab-2 and Lab-3, suggesting that the flow remained laminar for the Lab-1 at $Re_{throat}=2000$ but had transitioned to become turbulent for the other two laboratories. Consequently, the reattachment

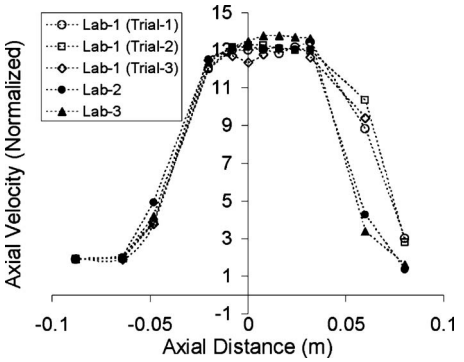

Fig. 10 Transitional flow data ($Re_{throat}=2000$): centerline velocity (normalized to the mean inlet velocity) versus axial distance

lengths were longer for Lab-1 trials in comparison to Lab-2 and Lab-3. While the exact recirculation lengths were not measured, the flow reattached around $\sim$15H for Lab-2 and Lab-3 and near $\sim$20H for Lab-1. This made the Lab-1 velocity profiles distinctly different from the Lab-2 and Lab-3 profiles at z=0.06 m (Fig. 11(*c*)); i.e., the jet remained separated from the wall for Lab-1, while it broke down and reattached to the wall for Lab-2. In Fig. 11(*c*), the interlaboratory uncertainty in centerline velocity measurement at this region was calculated to be $\sim 60\%$. This drastic increase in uncertainty levels while measuring transitional flows, especially near the reattachment region, is consistent with the results reported in previous studies [57–62], wherein the reattachment length in the transitional regime was shown to vary between 7H and 20H depending upon the inlet flow conditions. The reattachment lengths measured by the three laboratories fall within the range reported by previous studies.

The large variability in reattachment lengths and velocity data for $Re_{throat}=2000$ is possibly due to the high sensitivity and instability of the laminar to turbulent transition region, which is dependent on the Reynolds number and the amount of inlet flow disturbance. Our *error analysis* [Sec. 3.1] showed that the interlaboratory uncertainty in fluid property measurement and inlet velocity (and flow rate) was $\sim 10\%$. Consequently, the actual Reynolds numbers at which each laboratory performed the flow measurements were subject to an uncertainty of around 10%. To evaluate the sensitivity of the velocity profile to this Reynolds number variation, experiments were performed at Lab-1 in which velocity profiles were obtained for (i) $Re_{throat}=500$ and 500 ± 50

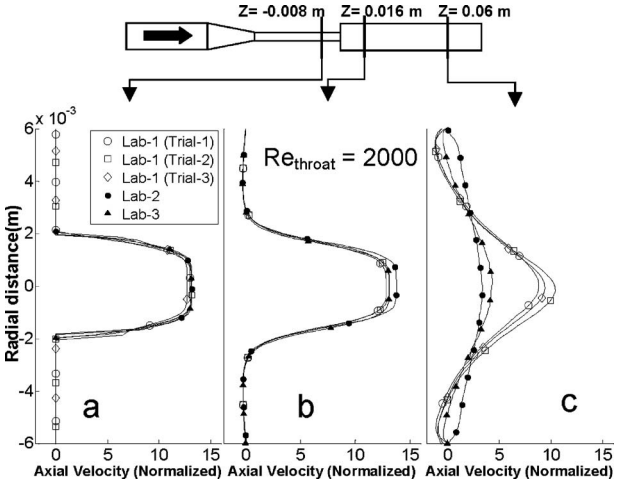

Fig. 11 Transitional flow data ($Re_{throat}=2000$): *velocity profiles at different cross-sections*

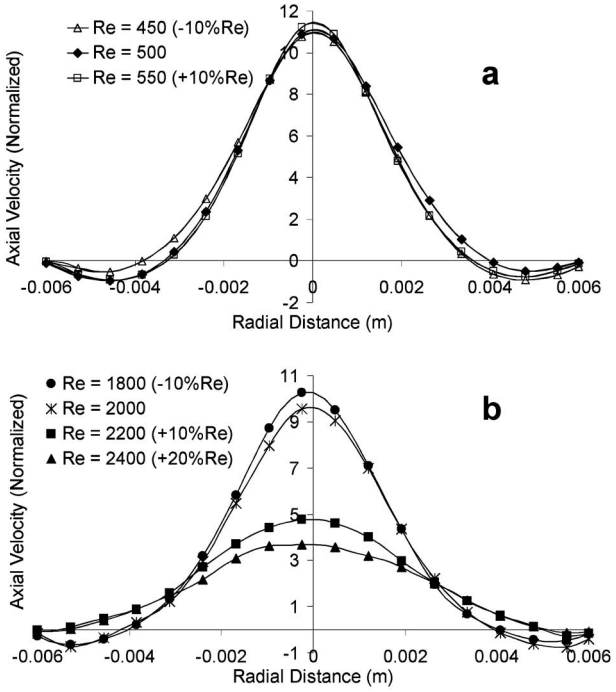

Fig. 12 Sensitivity of velocity profiles at z=0.06 m to Reynolds number uncertainty: (*a*) $Re_{throat}=500$ and (*b*) $Re_{throat}=2000$

and (ii) $Re_{throat}=2000$ and 2000 ± 200 (10% fluctuation of Re). When the flow was laminar ($Re_{throat}=500$), the 10% uncertainty in throat Reynolds number resulted in a less than 3% error in the centerline velocity downstream of the nozzle exit (Fig. 12(*a*)).

However, the same analysis performed for $Re_{throat}=2000$ produced a contrasting outcome (Fig. 12(*b*)). When Re_{throat} was increased to 2200 and 2400 (by increasing the flow rate), the jet broke down earlier and the velocity data (Fig. 12(*b*)) became similar to the Lab-2 and Lab-3 data obtained at $Re_{throat}=2000$ (Fig. 11(*c*)). In contrast, for a 10% drop in Re ($Re_{throat}=1800$), the velocity profile did not change significantly in relation to the $Re_{throat}=2000$ data (Fig. 12(*b*)). Hence, the transition region from laminar to turbulence was abrupt and very sensitive to the Reynolds number. In Fig. 12(*b*), a 10% variation in Reynolds number introduces ~55% uncertainty in the centerline velocity. Consequently, for the transitional flow ($Re_{throat}=2000$), the uncertainties in the fluid properties and flow rate measurements between laboratories (which was around 10%) could have caused the ~60% variation in centerline velocity observed at z=0.06 m (Fig. 11(*c*)).

Another possible source for this variation are the different levels of inlet flow disturbances measured by each laboratory (Fig. 7). Previous studies have reported that in the transitional flow regime ($Re_{throat}=2000$), the stability of the separated shear layer in the sudden expansion region and the reattachment process further downstream is significantly influenced by the amount of disturbance in the inlet flow [58–60,62]. Small perturbations in the inlet flow will be amplified in the shear layer downstream of the sudden expansion, and this instability can lead to an early breakdown of the jet. In our experiments, a measure of the upstream perturbations was the rms of the throat velocity measured by each laboratory. In the transitional regime ($Re_{throat}=2000$), the magnitude of the velocity fluctuations at the throat was ~12 times greater for Lab-2 and Lab-3, in comparison to values obtained at Lab-1. This difference in the upstream unsteadiness could be the reason for the flow remaining laminar for Lab-1 (at $Re_{throat}=2000$) but tipping over to the turbulent regime for Lab-2 and Lab-3.

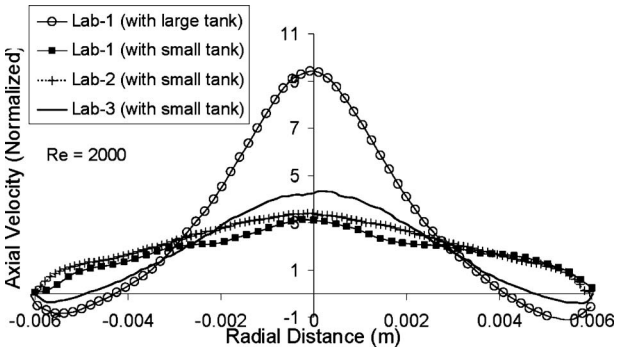

Fig. 13 Sensitivity of velocity profiles at z=0.06 m to upstream flow perturbations for $Re_{throat}=2000$

The volume of the mixing tank (stagnation chamber in Fig. 2) used by Lab-1 was ~4 times larger than the tanks used by Lab-2 and Lab-3 and may have helped to dampen the inlet disturbances. To check this hypothesis, experiments were repeated at Lab-1 using the smaller tank (used by Lab-2 and Lab-3). With this configuration, the flow transitioned to turbulence at z=0.06m similar to the other laboratories, and the interlaboratory centerline velocity matched within ~15% (Fig. 13).

3.3 Experimental Data Repository. The detailed PIV and CFD results are accessible through a downloadable program written in CodeGearTM Delphi® 2009 (Version 12.0.3210.17555).[4]

4 Discussion

Quantitative flow visualization is necessary to validate the results of CFD simulations. As part of FDA's efforts to improve the reliability of both PIV and CFD data as applied to medical devices, we initiated an interlaboratory study to characterize a benchmark nozzle model to better understand the practical limitations and error bounds associated with experimental PIV and to support current and future CFD simulations. The experimental data set[5] can assist in the validation of new CFD codes and for a better understanding of the existing codes. For example, for medical devices that produce flow characteristics similar to the features observed in the FDA nozzle device, the experimental results could be used to justify and validate the choice of different CFD solution parameters such as mesh density, mesh type, and turbulence model.

This study also established a standard operating procedure and a list of PIV best practices to maintain uniformity in the flow and boundary conditions among the testing laboratories while reducing the PIV measurement errors during quantitative flow visualization experiments. Results showed that for laminar ($Re_{throat}=500$) and turbulent ($Re_{throat}=3500$, 5000, and 6500) flow conditions (Figs. 8(*a*) and 9), the overall uncertainty in the interlaboratory centerline velocity measurements was ~10%. The possible causes for this variability, as pointed out in the error analysis [Sec. 3.1], were differences in the fluid property measurements, flow rate, PIV algorithms, and inlet boundary conditions. The cumulative error introduced by these sources was on the same order as the measured variability. The experimental uncertainties were much smaller than the size of the errors estimated from the round-robin CFD data. For example, at locations downstream of sudden expansion (for $Re_{throat}=500$), the standard deviation of the CFD data (from 28 different groups) was greater than 60% of the mean value, with only 4 out of 28 CFD results falling within the confidence intervals of the PIV data. The uncertainty in velocity mea-

[4]http://fdacfd.nci.nih.gov
[5]Available at http://fdacfd.nci.nih.gov

surement, though small, will still translate to errors in derived flow quantities such as viscous shear and Reynolds stresses, which could affect the accuracy of estimates of blood damage.

However, following the SOP did not eliminate the large uncertainties in the velocity measurements for the transitional flow regime (Re_{throat}=2000), especially near the reattachment region (Figs. 10 and 11). Our sensitivity analysis (Figs. 12 and 13) showed that minimizing the uncertainty in the Reynolds number to less than ~5% and matching inlet perturbations are critical to achieving good reproducibility in the transitional flow regime. By matching the inlet rms perturbation levels for all three laboratories, the interlaboratory uncertainty in centerline velocity decreased from ~60% to ~15%. It should be noted that as part of the original SOP, the mean velocity and the symmetry of the velocity profile at the model inlet was matched, but no effort was made to maintain uniformity in the inlet perturbation levels across the laboratories. This was to ensure fair comparison with the CFD round-robin data for which the inlet turbulent intensity level was not stipulated as part of the boundary conditions. However, for future PIV and CFD interlaboratory evaluations of benchmark models, the inlet conditions need to be better specified.

The large error bars in velocity data for Re_{throat}=2000 near the reattachment region is not indicative of the PIV technique's inability to measure transitional flows accurately. Rather, this measurement is a testament to the sensitivity of the transitional flow, especially in the presence of flow separation, to the inlet perturbations. The unpredictability of the flow in the transition region can introduce large uncertainties in quantities such as residence time, shear stresses, and Reynolds stresses experienced by blood cells. Since jet flows and recirculation regions have been linked to hemolysis and platelet deposition [63], it will be useful to study how the differences in the recirculation lengths and velocity profiles, caused by variations in flow conditions, affect the estimated blood damage potential of the device.

While the SOP was developed with the simple nozzle model in mind, several aspects of it (listed in Table 3) such as fluid property and flow control and the PIV *best practices* are still applicable to flow measurements in medical devices. Furthermore, it can be extended to actual medical devices with some modifications. For example, the flow loop (Fig. 2) and the flow conditions (steady or pulsatile flow) for testing a medical device should be more physiological. While we maintained fully developed flow at the inlet of the nozzle model (Fig. 6), a range of clinically relevant inlet and exit boundary conditions should be used to evaluate new medical devices as fully developed flow may not be relevant to a given device under study. Moreover, while we suppressed cavitation from occurring in the model during the testing by increasing the system pressure, its occurrence must be evaluated in actual medical devices. In the future, the SOP will be followed to test a more realistic medical device model, such as a simplified ventricular assist device, and will be modified based on the feedback from the results.

This paper presented the experimental testing protocol, the PIV best practices, and some of the interlaboratory derived velocity data while evaluating the variability in the centerline velocity at different cross-sections in the sudden expansion orientation. Our future studies will focus on the experimental data obtained from the conical diffuser orientation (i.e., when the flow direction was reversed in the nozzle model). In general, the interlaboratory uncertainties in centerline velocity in the conical diffuser orientation were comparable to the uncertainty levels encountered in the sudden expansion orientation. In the future, we will also present the interlaboratory results for other flow variables such as recirculation velocity, jet widths, and viscous and Reynolds stresses and quantify the uncertainties in measuring the velocities in the near-wall and low-flow recirculation regions, where PIV typically performs poorly. Since predictions of blood damage are related nonlinearly to the flow quantities such as cellular dwell time and shear stresses [64], we will also focus on studying how the interlaboratory uncertainties in flow quantities translate to uncertainties in blood damage predictions. Results from the uncertainty analysis will be used to evaluate the limits of applicability of PIV results, especially the use of PIV determined velocity and shear and Reynolds stresses in validating CFD simulations and in determining the safety of medical devices.

5 Conclusions

Through this FDA-sponsored study, a standard methodology for performing quantitative flow visualization studies in a benchmark nozzle model with flow characteristics similar to a variety of blood-contacting medical devices was collaboratively developed. The study results demonstrated that our standard operating procedure reduced a significant amount of measurement error and interlaboratory variability in velocity measurements, especially in laminar and turbulent flow regimes. The study also showed the limitations in making velocity measurements in the transitional flow regime where inlet flow disturbances and variable flow properties may affect the downstream flow characteristics and hence the experimental results. The best practices described in this study for performing these types of experiments may help to enhance the accuracy of the PIV data and increase the reliability of CFD analyses in the device review process. Future studies will focus on improving the SOP to further minimize errors in measuring flow parameters more relevant to device safety, such as near-wall velocity, wall shear stress, and Reynolds stress.

Nomenclature

- D = nozzle inlet diameter
- H = step height (difference between exit pipe radius and throat radius) (=4 mm)
- P_z = static pressure measured at location z
- Q = experimental flow rate
- Re_{throat} = Reynolds number measured based on the nozzle throat diameter (=4 mm)
- Re_{inlet} = Reynolds number measured based on the nozzle inlet diameter (=12 mm)
- SI = symmetry index
- r_{inlet} = radius of the nozzle inlet (=6 mm)
- r_{throat} = radius of the nozzle throat (=2 mm)
- u_{NaI} = axial velocity of the blood analog fluid measured from PIV experiment
- u_{blood} = axial velocity of the blood estimated from scaling u_{NaI} using Reynolds number similarity
- $u_{normalized}$ = normalized axial velocity (with respect to the mean inlet velocity)
- $\bar{u}_{inlet}$ = mean inlet velocity
- $\bar{u}_{throat}$ = mean throat velocity
- z = axial distance
- Δt = time difference between two frames of a PIV image pair
- ΔP = pressure difference measured relative to the pressure at z=0
- $\Delta P_{normalized}$ = ΔP normalized with respect to the mean throat velocity ($\bar{u}_{throat}$)
- λ = wavelength of the PIV laser
- μ_{blood} = dynamic viscosity of the blood
- μ_{NaI} = dynamic viscosity of the blood analog fluid (NaI solution)
- ρ_{blood} = density of the blood
- ρ_{NaI} = density of the blood analog fluid (NaI solution)
- τ_{NaI} = viscous shear stress magnitude of the blood analog fluid calculated from the PIV measured velocity
- τ_{blood} = viscous shear stress magnitude of the blood estimated from scaling τ_{NaI} using Reynolds number similarity

τ'_{NaI} = Reynolds stress magnitude of the blood analog fluid calculated from the PIV measured velocity

τ'_{blood} = Reynolds stress magnitude of the blood estimated from scaling τ'_{NaI} using Reynolds number similarity

References

[1] Pinotti, M., and Rosa, E. S., 1995, "Computational Prediction of Hemolysis in a Centrifugal Ventricular Assist Device," Artif. Organs, **19**(3), pp. 267–273.

[2] Grigioni, M., Daniele, C., D'Avenio, G., and Barbaro, V. A., 1999, "Discussion on the Threshold Limit for Hemolysis Related to Reynolds Shear Stress," J. Biomech., **32**, pp. 1107–1112.

[3] Burgreen, G. W., Antaki, J. F., Wu, Z. J., and Holmes, A. J., 2001, "Computational Fluid Dynamics as a Development Tool for Rotary Blood Pumps," Artif. Organs, **25**(5), pp. 336–340.

[4] De Wachter, D., and Verdonck, P., 2002, "Numerical Calculation of Hemolysis Levels in Peripheral Hemodialysis Cannulas," Artif. Organs, **26**(7), pp. 576–582.

[5] Yano, T., Sekine, K., Mitoh, A., Mitamura, Y., Okamoto, E., Kim, D. W., Nishimura, I., Murabayashi, S., and Yozu, R., 2003, "An Estimation Method of Hemolysis Within an Axial Flow Blood Pump by Computational Fluid Dynamics Analysis," Artif. Organs, **27**(10), pp. 920–925.

[6] Arvand, A., Hormes, M., and Reul, H., 2005, "A Validated Computational Fluid Dynamics Model to Estimate Hemolysis in a Rotary Blood Pump," Artif. Organs, **29**(7), pp. 531–540.

[7] Behbahani, M., Behr, M., Hormes, M., Steinseifer, U., Arora, D., Coronado, O., and Pasquali, M., 2009, "A Review of Computational Fluid Dynamics Analysis of Blood Pumps," Eur. J. Appl. Math., **20**(04), pp. 363–397.

[8] Wootton, D. M., Markou, C. P., Hanson, S. R., and Ku, D. N., 2001, "A Mechanistic Model of Acute Platelet Accumulation in Thrombogenic Stenoses," Ann. Biomed. Eng., **29**(4), pp. 321–329.

[9] Goodman, P. D., Barlow, E. T., Crapo, P. M., Mohammad, S. F., and Solen, K. A., 2005, "Computational Model of Device-Induced Thrombosis and Thromboembolism," Ann. Biomed. Eng., **33**(6), pp. 780–797.

[10] Sorensen, E. N., Burgreen, G. W., Wagner, W. R., and Antaki, J. F., 1999, "Computational Simulation of Platelet Deposition and Activation: I. Model Development and Properties," Ann. Biomed. Eng., **27**, pp. 436–448.

[11] Fallon, A. M., Dasi, L. P., Marzec, U. M., Hanson, S. R., and Yoganathan, A. P., 2008, "Procoagulant Properties of Flow Fields in Stenotic and Expansive Orifices," Ann. Biomed. Eng., **36**(1), pp. 1–13.

[12] Tamagawa, M., Kaneda, H., Hiramoto, M., and Nagahama, S., 2009, "Simulation of Thrombus Formation in Shear Flows Using Lattice Boltzmann Method," Artif. Organs, **33**(8), pp. 604–610.

[13] Richardson, E., 1975, "Applications of a Theoretical Model for Haemolysis in Shear Flow," Biorheology, **12**(1), pp. 27–37.

[14] Giersiepen, M., Wurzinger, L. J., Opitz, R., and Reul, H., 1990, "Estimation of Shear Stress-Related Blood Damage in Heart Valve Prostheses—In Vitro Comparison of 25 Aortic Valves," Int. J. Artif. Organs, **13**(5), pp. 300–306.

[15] Bludszuweit, C., 1995, "Model for a General Mechanical Blood Damage Prediction," Artif. Organs, **19**(7), pp. 583–589.

[16] Gu, L., and Smith, W., 2005, "Evaluation of Computational Models for Hemolysis Estimation," ASAIO J., **51**(3), pp. 202–207.

[17] Hentschel, B., Tedjo, I., Probst, M., Wolter, M., Behr, M., Bischof, C., and Kuhlen, T., 2008, "Interactive Blood Damage Analysis for Ventricular Assist Devices," IEEE Trans. Vis. Comput. Graph., **14**(6), pp. 1515–1522.

[18] http://www.fda.gov/ScienceResearch/SpecialTopics/CriticalPathInitiative/UCM076689.htm

[19] Stewart, S. F. C., Day, S., Burgreen, G. W., Paterson, E. G., Manning, K. B., Hariharan, P., Deutsch, S., Giarra, M., Cheek, C., Reddy, V., Berman, M., Myers, M. R., and Malinauskas, R. A., 2009, "Preliminary Results of FDA's 'Critical Path' Project to Validate Computational Fluid Dynamic Methods Used in Medical Device Evaluation," ASAIO J., **55**(2), p. 173.

[20] Browne, P., Ramuzat, A., Saxena, R., and Yoganathan, A. P., 2000, "Experimental Investigation of the Steady Flow Downstream of the St. Jude Bileaflet Heart Valve: A Comparison Between Laser Doppler Velocimetry and Particle Image Velocimetry Techniques," Ann. Biomed. Eng., **28**(1), pp. 39–47.

[21] Kaminsky, R., Morbiducci, U., Rossi, M., Scalise, L., Verdonck, P., and Grigioni, M., 2007, "Time-Resolved PIV Technique for High Temporal Resolution Measurement of Mechanical Prosthetic Aortic Valve Fluid Dynamics," Int. J. Artif. Organs, **30**(2), pp. 153–162.

[22] Kaminsky, R., Dumont, K., Weber, H., Schroll, M., and Verdonck, P., 2007, "PIV Validation of Blood-Heart Valve Leaflet Interaction Modelling," Int. J. Artif. Organs, **30**(7), pp. 640–648.

[23] Manning, K. B., Kini, V., Fontaine, A. A., Deutsch, S., and Tarbell, J. M., 2003, "Regurgitant Flow Field Characteristics of the St. Jude Bileaflet Mechanical Heart Valve Under Physiologic Pulsatile Flow Using Particle Image Velocimetry," Artif. Organs, **27**(9), pp. 840–846.

[24] Lim, W. L., Chew, Y. T., Chew, T. C., and Low, H. T., 2001, "Pulsatile Flow Studies of a Porcine Bioprosthetic Aortic Valve In Vitro: PIV Measurements and Shear-Induced Blood Damage," J. Biomech., **34**, pp. 1417–1427.

[25] Ge, L., Dasi, L. P., Sotiropoulos, F., and Yoganathan, A. P., 2008, "Characterization of Hemodynamic Forces Induced by Mechanical Heart Valves: Reynolds vs. Viscous Stresses," Ann. Biomed. Eng., **36**(2), pp. 276–297.

[26] Engelmayr, G. C., Jr., Soletti, L., Vigmostad, S. C., Budilarto, S. G., Federspiel, W. J., Chandran, K. B., Vorp, D. A., and Sacks, M. S., 2008, "A Novel Flex-Stretch-Flow Bioreactor for the Study of Engineered Heart Valve Tissue Mechanobiology," Ann. Biomed. Eng., **36**(5), pp. 700–712.

[27] Hochareon, P., Manning, K. B., Fontaine, A. A., Tarbell, J. M., and Deutsch, S., 2004, "Wall Shear-Rate Estimation Within the 50cc Penn State Artificial Heart Using Particle Image Velocimetry," ASME J. Biomech. Eng., **126**, pp. 430–437.

[28] Deutsch, S., Tarbell, J. M., Manning, K. B., Rosenberg, G., and Fontaine, A. A., 2006, "Experimental Fluid Mechanics of Pulsatile Artificial Blood Pumps," Annu. Rev. Fluid Mech., **38**, pp. 65–86.

[29] Day, S. W., and McDaniel, J. C., 2005, "PIV Measurements of Flow in a Centrifugal Blood Pump: Steady Flow," ASME J. Biomech. Eng., **127**(2), pp. 244–253.

[30] Day, S. W., and McDaniel, J. C., 2005, "PIV Measurements of Flow in a Centrifugal Blood Pump: Time-Varying Flow," ASME J. Biomech. Eng., **127**(2), pp. 254–263.

[31] Shu, F., Vandenberghe, S., and Antaki, J. F., 2009, "The Importance of dQ/dt on the Flow Field in a Turbodynamic Pump With Pulsatile Flow," Artif. Organs, **33**(9), pp. 757–762.

[32] Lee, H., Tatsumi, E., and Taenaka, Y., 2009, "Experimental Study on the Reynolds and Viscous Shear Stress of Bileaflet Mechanical Heart Valves in a Pneumatic Ventricular Assist Device," ASAIO J., **55**(4), pp. 348–354.

[33] Medvitz, R. B., Reddy, V., Deutsch, S., Manning, K. B., and Paterson, E. G., 2009, "Validation of a CFD Methodology for Positive Displacement LVAD Analysis Using PIV Data," ASME J. Biomech. Eng., **131**(11), p. 111009.

[34] Cooper, B. T., Roszelle, B. N., Long, T. C., Deutsch, S., and Manning, K. B., 2010, "The Influence of Operational Protocol on the Fluid Dynamics in the 12 cc Penn State Pulsatile Pediatric Ventricular Assist Device: The Effect of End-Diastolic Delay," Artif. Organs, **34**(4), pp. E122–E133.

[35] Benard, N., Coisne, D., Donal, E., and Perrault, R., 2003, "Experimental Study of Laminar Blood Flow Through an Artery Treated by a Stent Implantation: Characterisation of Intra-Stent Wall Shear Stress," J. Biomech., **36**, pp. 991–998.

[36] Charonko, J., Karri, S., Schmieg, J., Prabhu, S., and Vlachos, P., 2009, "In Vitro, Time-Resolved PIV Comparison of the Effect of Stent Design on Wall Shear Stress," Ann. Biomed. Eng., **37**(7), pp. 1310–1321.

[37] Stanislas, K., Okamoto, K., Kahler, C. J., Westerweel, J., and Scarano, F., 2008, "Main Results of the Third International Challenge," Exp. Fluids, **45**, pp. 27–71.

[38] Umezu, M., Fujimasu, H., Yamada, T., Fujimoto, T., Ranawake, M., Nogawa, A., and Kijima, T., 1996, "Fluid Dynamic Investigation of Mechanical Blood Hemolysis," Proceedings of the Fifth International Symposium on Artificial Heart and Assist Devices, pp. 327–335.

[39] Hinds, M. T., Park, Y. J., Jones, S. A., Giddens, D. P., and Alevriadou, B. R., 2001, "Local Hemodynamics Affect Monocytic Cell Adhesion to a Three-Dimensional Flow Model Coated With E-Selectin," J. Biomech., **34**(1), pp. 95–103.

[40] Worth Longest, P., and Kleinstreuer, C., 2003, "Comparison of Blood Particle Deposition Models for Non-Parallel Flow Domains," J. Biomech., **36**(3), pp. 421–430.

[41] Kameneva, M. V., Burgreen, G. W., Kono, K., Repko, B., Antaki, J. F., and Umezu, M., 2004, "Effects of Turbulent Stresses Upon Mechanical Hemolysis: Experimental and Computational Analysis," ASAIO J., **50**, pp. 418–423.

[42] Lacasse, D., Garon, A., and Pelletier, D., 2007, "Mechanical Hemolysis in Blood Flow: User-Independent Predictions With the Solution of a Partial Differential Equation," Comput. Methods Biomech. Biomed. Eng., **10**(1), pp. 1–12.

[43] Prasad, A. K., 2000, "Particle Image Velocimetry," Curr. Sci., **79**(1), pp. 51–60.

[44] Westerweel, J., 1993, "Digital Particle Image Velocimetry, Theory and Application," Ph.D. thesis, Delft University Press, Delft, The Netherlands.

[45] Westerweel, J., 1997, "Fundamentals of Digital Particle Image Velocimetry," Meas. Sci. Technol., **8**, pp. 1379–1392.

[46] LaVision Inc., 2008, DAVIS FLOWMASTER Software Manual.

[47] Keane, R. D., and Adrian, R. J., 1992, "Theory of Cross-Correlation Analysis of PIV Images," Appl. Sci. Res., **49**, pp. 191–215.

[48] Huang, H., Dabiri, D., and Gharib, M., 1997, "On Errors of Digital Particle Image Velocimetry," Meas. Sci. Technol., **8**, pp. 1427–1440.

[49] Christensen, K. T., 2004, "The Influence of Peak-Locking Errors on Turbulence Statistics Computed From PIV Ensembles," Exp. Fluids, **36**, pp. 484–497.

[50] Nobach, H., and Bodenschatz, E., 2009, "Limitations of Accuracy in PIV Due to Individual Variations of Particle Image Intensities," Exp. Fluids, **47**, pp. 27–38.

[51] Hariharan, P., Myers, M. R., Robinson, R. A., Maruvada, S. H., Sliwa, J., and Banerjee, R. K., 2008, "Characterization of High Intensity Focused Ultrasound Transducers Using Acoustic Streaming," J. Acoust. Soc. Am., **123**(3), pp. 1706–1719.

[52] Zhou, M., and Garner, C. P., 1996, "Particle Image Velocimetry Measurements of the Flow Field Within an Enclosed Rotating Disc-Stator System and Comparison With Computational Fluid Dynamics Results," Optical Diagnostics in Engineering, **1**(2), pp. 9–21.

[53] Adrian, R. J., 1997, "Dynamic Ranges of Velocity and Spatial Resolution of Particle Image Velocimetry," Meas. Sci. Technol., **8**, pp. 1393–1398.

[54] Nigen, S., El Kissi, N., Piau, J. M., and Sadun, S., 2003, "Velocity Field for Polymer Melts Extrusion Using Particle Image Velocimetry Stable and Un-

stable Flow Regimes," J. Non-Newtonian Fluid Mech., **112**, pp. 177–202.
[55] Wernet, M. P., Subramanian, A., Mu, H., and Kadambi, J. R., 2000, "Comparison of Particle Image Velocimetry and Laser Doppler Anemometry Measurements in Turbulent Fluid Flow," Ann. Biomed. Eng., **28**, pp. 1393–1394.
[56] Hinze, J. O., 1975, *Turbulence*, 2nd ed., McGraw-Hill, New York.
[57] Gach, M. H., and Lowe, I. J., 2000, "Measuring Flow Reattachment Lengths Downstream of a Stenosis Using MRI," J. Magn. Reson Imaging, **12**, pp. 939–948.
[58] Pak, B., Cho, Y. I., and Choi, S. U. S., 1990, "Separation and Reattachment of Non-Newtonian Fluid Flows in a Sudden Expansion Pipe," J. Non-Newtonian Fluid Mech., **37**, pp. 175–199.
[59] Cantwell, C. D., Barkley, D., and Blackburn, H. M. 2010, "Transient Growth Analysis of Flow Through a Sudden Expansion in a Circular Pipe," Phys. Fluids, **22**, p. 034101.
[60] Mehrez, Z., Bouterra, M., Cafsi, A. E., Belghith, A., and Le Quere, P., 2009, "The Influence of the Periodic Disturbance on the Local Heat Transfer in Separated and Reattached Flow," Heat Mass Transfer, **46**, pp. 107–112.
[61] Armaly, B. F., Durst, F., Pereira, J. C. F., and Schönung, B., 1983, "Experimental and Theoretical Investigation of Backward-Facing Step Flow," J. Fluid Mech., **127**, pp. 473–496.
[62] Sreenivasan, K. R., 1983, "Some Studies of Non-Simple Pipe Flows," Trans. of the Institution of Engineers, Australia: Mech. Eng., **8**, pp. 200–208.
[63] Bluestein, D., Niu, L., Schoephoerster, R. T., and Dewanjee, M. K., 1997, "Fluid Mechanics of Arterial Stenosis: Relationship to the Development of Mural Thrombus," Ann. Biomed. Eng., **25**, pp. 344–356.
[64] Leverett, L. B., Hellums, J. D., Alfrey, C. P., and Lynch, E. C., 1972, "Red Blood Cell Damage by Shear Stress," Biophys. J., **12**, pp. 257–273.
[65] Scarano, F., and Riethmuller, M., 1999, "Iterative Multigrid Approach in PIV Image Processing With Discrete Window Offset," Exp. Fluids, **26**, pp. 513–523.